Article

Characteristics of Very Large-Scale Motions in Rough-Bed Open-Channel Flows

Ying Shen [ID], Shengfa Yang and Jie Liu *

National Inland Waterway Regulation Engineering Research Center, Chongqing Jiaotong University, Chongqing 400074, China; shenying@cqjtu.edu.cn (Y.S.); ysf777@163.com (S.Y.)
* Correspondence: from_mars@126.com

Abstract: Rough-bed open-channel flows (OCFs) are ubiquitous in rivers and canals. However, the scaling and energy contents of very-large-scale motions (VLSMs) in such flows remain unclear. In this study, the above characteristics of VLSMs are experimentally investigated with the measurement of particle imaging velocimetry (PIV). VLSM wavelengths obtained via premultiplied spectra analysis were consistent with previously reported values. Comparisons with these studies ruled out the role of relative submergence, and suggested that the channel aspect ratio is key to controlling the VLSM wavelengths in OCFs. VLSMs carry approximately 60% of the turbulence kinetic energy (TKE) and 38–50% of the Reynolds stress in rough-bed OCFs. The VLSM-related TKE fraction in the 0.1–0.5H range increased with increasing friction Reynolds number, while variation in the Reynolds shear stress did not exhibit any explicit trend.

Keywords: very-large-scale motion; premultiplied spectra; open-channel flow; large submergence

1. Introduction

The existence of very-large-scale motions (VLSMs) with wavelengths of O (10H) (where H refers to the pipe radius, channel half-height boundary, layer thickness or water depth in different flows) was confirmed in various wall-bounded flows, including pipe flows (PFs) [1–5], closed-channel flows (CCFs) [1,4], turbulent boundary layers (TBLs) [2,4,6] and open-channel flows (OCFs) [7–11]. As a class of turbulent structures, VLSMs are both energetic and stress-active, carrying about half of the turbulence energy and Reynolds shear stress in smooth-bed PFs, CCFs, TBLs, and OCFs [4,5,8]. Probably due to the above feature, VLSMs play an important role in particle entrainment and sediment transport [12–14]. Though hydraulic engineering often deals with rough-bed OCFs, most VLSM studies have focused on smooth-walled conditions. To further clarify the role of VLSMs in the transport of momentum, energy, and mass, further understanding the characteristics of VLSMs over rough-bed OCFs is necessary.

The differences between OCFs and other types of wall-bounded turbulent flows with regard to VLSMs have been partly revealed. For example, VLSMs appear at a much lower friction Reynolds number Re_τ and persist farther into the outer layers in OCFs than they do in other flows [9]. Similarly, whether different wall types in terms of a smooth or rough bed make a difference is another question. VLSMs, having only been documented rather recently, in the past two decades, still have many open questions, such as regarding their origin, scaling, and dynamics. This study attempts to explore VLSMs in OCFs regarding their scaling and energy contents. Compared with flows over a smooth bed, OCFs over a rough bed are much more complex. In addition to the general impact of Re_τ on turbulent flows, a rough bed introduces other parameters, including relative submergence H/Δ (where Δ refers to the equivalent roughness) and roughness Reynolds number Re_Δ, and their relevance to VLSMs is still debated.

The scales of VLSMs in OCFs were first tackled by Cameron et al. [11]. On the basis of premultiplied spectrum analysis, they reported that the relative VLSM wavelength to H is

not invariable and shows a dependence on channel aspect ratio B/H (where B refers to the channel width), H/Δ, or Re_τ. However, they could not identify the dominant contributing factor because their experiments maintained the B/H ratio and Re_Δ constant. To further explore the scaling of VLSMs, Peruzzi et al. [9] conducted experiments under nonuniform flow conditions over a smooth bed and indicated the B/H ratio as the key scale among the B/H ratio, Re_τ, and the nondimensional distance from flume inlet x/H. Because their experiments were performed in smooth-wall conditions, whether relative submergence plays a role in controlling the scaling of VLSMs remains unclear. Providing an answer to this question is one of the main objectives of the present study.

The energy contents of VLSMs in OCFs were reported for the first time by Duan et al. [8]. They demonstrated that over 50% of the turbulent kinetic energy (TKE) and Reynolds shear stress is carried by VLSMs in a uniform smooth-bed OCF. Later, there were reports of corresponding quantities in nonuniform OCFs, such as decelerating OCFs [10] and OCFs upstream of a run-of-river dam [7]. However, all these studies were undertaken in smooth-wall conditions. Similar studies for rough-bed OCFs are still lacking.

This study aims to elucidate the scaling of VLSMs, and their contributions to TKE and Reynolds shear stress in rough-bed OCFs. A better understanding of VLSMs would help in addressing engineering challenges such as sediment transport, pollutant dispersion, and hydraulic resistance. The remainder of this paper is organized as follows. Section 2 describes the experimental setup and data-processing methods. Section 3 summarizes the bulk statistics and spectral analysis results. Lastly, the main findings are briefly outlined in Section 4.

2. Experiments

2.1. Experimental Setup

The experiments were conducted in a recirculating open-channel flume using high-speed two-dimensional (2D) PIV. The flume was 12 m long, 0.25 m wide, and 0.25 m high (Figure 1a). The channel slope could be modulated using an adjustment wheel under the flume. Its bed and sidewalls were all composed of ultraclear glass to enable flexible PIV measurements. The flow was driven by a pump, and the flow discharge was monitored using an electromagnetic flowmeter. Three honeycombs were placed at the entrance to the flume to ensure no large-scale flow structures during the recirculation process. A tailgate regulating the backwater curve is located at the end of the flume. Four ultrasonic level sensors were installed along the flume to monitor the streamwise variation in water depth, so as to maintain the flow uniform in all runs. The measurements were conducted in a wall-normal streamwise plane in the middle of the channel and were located 8 m ($>150H$) downstream of the flume entrance. This distance was sufficient for ensuring fully developed flow conditions over the rough beds [15]. To ensure 2D flow in the observed plane, B/H should be above 5 [16], corresponding to the maximal water depth of 5 cm in this study. The channel bed was roughened with a layer of 4 mm diameter glass spheres. The spherical particles were in a hexagonal close-packed arrangement using perforated stainless-steel plates.

A 1.5 mm thick laser sheet, generated using a continuous-wave 10 W laser, was used to illuminate the field of view. A thin plexiglass sheet with a streamlined plane shape [17] was used to prevent image distortion because of water surface undulations at large flow velocities. It was located at the water surface, and the laser light entered the water through it. A complementary high-speed metal-oxide-semiconductor (CMOS) camera (DHI Phantom-Miro-M340, 12G, 2560 × 1920 pixels) was used to capture flow images with a Tamron 90 mm f/2.8 D lens. Flow tracers were polyamide resin particles (mean diameter, 20 μm; density, 1.03–1.04 g/cm^3). The particle images were postprocessed using PIVlab, graphical user interface (GUI)-based PIV software of which the accuracy verification can be found in the literature [18]. The initial interrogation window size was 64 × 64 pixels, and the final window, with 2–4 particles, was 16 × 16 pixels after three passes with a 50% overlap. The

accuracy of the resulting velocity vectors was verified using the three standard deviations of the fluctuation velocity. Bad vectors constituted less than 1% for all the flow fields.
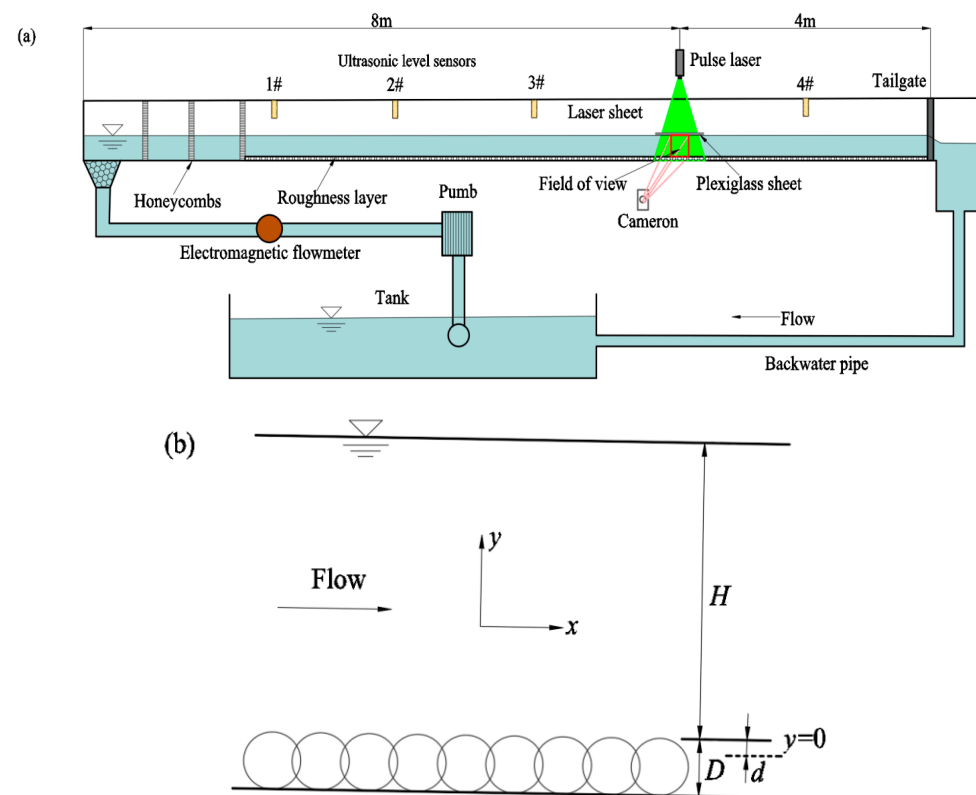

Figure 1. (**a**) Schematic of the open-channel flume. (**b**) Definitions of flow depth H and zero-plane displacement d.

A two-dimensional coordinate system was adopted in this study, that is, x and y represent the streamwise and wall-normal directions, respectively. The time-averaged velocities along the corresponding directions are denoted by U and V, with fluctuating velocities denoted by u and v. The + superscript indicates normalized quantities by friction velocity u_* and kinematic viscosity ν, such as $U^+ = U/u_*$ and $\Delta x^+ = \Delta x u_*/\nu$. The prime symbol indicates the root mean square, so the turbulence intensities of the streamwise and wall-normal velocities are u' and v', respectively.

The flow conditions for all the runs are detailed in Table 1. Given the important role that Re_τ plays in wall turbulence, the friction Reynolds number differed for different runs. Taking into account that B/H and H/Δ are also possible key parameters in controlling the scaling of VLSMs [19], different values were set for Runs R1–R3. Friction velocity u_* was determined on the basis of the log law. All of the experiments were conducted under fully developed rough and subcritical flow conditions ($Fr < 1$). Equivalent roughness $\Delta = 0.67D$ [20] (where D is the particle diameter) was assumed in this study, and $H/\Delta > 5$ for all runs indicates that all of the flows in this study had large submergence [21].

The PIV measurement parameters are listed in Table 2. The frequency of the velocity fields was set to conform to the 1/4 rule [22]. ΔT^+ was generally less than 1–3 to resolve the small-scale turbulent motions [23] in all runs except for R2, in which ΔT^+ was even larger than 5. Therefore, the results for R2 were not used to analyze the fraction of TKE and the Reynolds stress carried by VLSMs owing to its mismatched resolving ability with other runs. The streamwise distance of mean flow movement TU_m was above $1000H$, which was sufficiently long to yield convergent spectral results.

Table 1. Flow conditions [a].

Run	J	ν $(10^{-6}\mathrm{m}^2/\mathrm{s})$	H (cm)	U_m (m/s)	u_* (cm/s)	B/H	H/D	H/Δ	Fr	Re	Re_τ	Re_Δ
R1	0.003	0.88	1.73	0.25	2.25	14.5	4.33	6.49	0.61	4964	442	68
R2	0.002	0.84	2.87	0.27	2.17	8.7	7.17	10.76	0.50	9156	742	69
R3	0.001	0.88	4.88	0.21	1.50	5.1	12.19	18.28	0.30	11,393	831	46
R4	0.003	0.85	4.86	0.45	3.30	5.1	12.14	18.21	0.65	25,601	1879	104
R5	0.005	0.87	4.92	0.60	4.50	5.1	12.30	18.45	0.87	34,008	2537	138

Notes: [a] J = bed slope, ν = kinematic viscosity, H = water depth above the roughness tops, U_m = depth-averaged velocity, u_* = friction velocity, B/H = flow aspect ratio, H/Δ = relative submergence, $Fr = U_m/(gH)^{0.5}$ = Froude number, $Re = U_m H/\nu$ = Reynolds number, $Re_\tau = u_* H/\nu$ = friction Reynolds number, and $Re_\Delta = u_*\Delta/\nu$ = roughness Reynolds number.

Table 2. PIV parameters [b].

Run	Image Size (Pixels)	Resolution (Pixels/mm)	F_s (Hz)	ΔT^+	$\Delta T U_\mathrm{m}/H$	No. of Image Pairs	$T U_\mathrm{m}/H$	$\Delta x^+/\Delta y^+$
R1	128×640	30.77	600	0.96	0.024	$19,268 \times 3$	1407	6.64
R2	128×560	17.43	100	5.61	0.093	$109,784 \times 3$	15,360	23.4
R3	128×1600	30.77	600	0.43	0.007	$38,513 \times 20$	5418	4.43
R4	128×1600	30.77	1200	1.06	0.008	$38,513 \times 12$	3566	10.06
R5	128×1600	30.77	1400	1.66	0.009	$38,513 \times 20$	6744	13.41

Notes: [b] F_s = sampling frequency of the velocity fields, $\Delta T = 1/Fs$ = time interval between successive velocity fields, T = total image acquisition time, Δx^+ or Δy^+ = inner-scaled vector spacing in the streamwise or wall-normal direction.

2.2. Methods

Spectral analysis is commonly used in turbulence studies to obtain the energy distribution across different frequencies and wavenumbers (or wavelengths) [5,24–27]. The power spectral density $S_{u_i u_j}(f)$ in the frequency domain could be obtained by computing the discrete Fourier transform (FT) of the fluctuating velocity signal as follows:

$$S_{u_i u_j}(f) = C \left| F_{u_i}(f) F_{u_j}{}^*(f) \right| \tag{1}$$

where f is the frequency; $F_{u_i}(f)$ is the FT of u_i ($u_1 = u$, $u_2 = v$); * and $|\ |$ indicate the complex conjugate and modulus, respectively; C is a constant determined by satisfying equation $\overline{u_i u_j} = \int_0^\infty S_{u_i u_j}(f)df$.

The frequency-based $S_{u_i u_j}(f)$ can be transformed into wavenumber-based spectral density $S_{u_i u_j}(k_x)$ by using Taylor's frozen turbulence hypothesis [28] through the following relationship:

$$k_x = \frac{2\pi f}{U(y)} \tag{2}$$

where k_x is the streamwise wavenumber related to wavelength λ by $\lambda = 2\pi/k_x$, and $U(y)$ is the time-averaged streamwise velocity at y. The relationship between these two spectral densities is as follows:

$$S_{u_i u_j}(k_x) = \frac{U(y)}{2\pi} S_{u_i u_j}(f) \tag{3}$$

Similar to $S_{u_i u_j}(f)$, $S_{u_i u_j}(k_x)$ satisfies equation $\overline{u_i u_j} = \int_0^\infty S_{u_i u_j}(k_x)dk_x$. It can be easily deduced that $\overline{u^2} = \int_0^\infty S_{uu}(k_x)dk_x = \int_0^\infty k_x S_{uu}(k_x)d(\ln k_x)$. Given that $\overline{u^2}/2$ was exactly the mean streamwise TKE, the area enclosed by the curve of $k_x S_{uu}(k_x)$ plotted in single logarithmic coordinates with the horizontal coordinate was equal to twice the streamwise TKE. Similar conclusions could be drawn regarding the wall-normal TKE and Reynolds stress.

The magnitude of the premultiplied spectra reflects the mean contribution of the turbulent motions at the corresponding wavenumber (or wavelength) to TKE or Reynolds stress. To achieve the instantaneous strength of these motions, time-frequency analysis such

as wavelet or wavelet-Hilbert analysis could be performed (e.g., Wickersham et al. [29], Li and Li [30], Mariotti [31], Perna et al. [32]) to highlight when the dominant frequencies or scales occur. No extra wavelet analysis was carried out because we focused on the average performance of VLSMs in this study.

Given that Taylor's hypothesis may distort the true wavenumber spectrum in the $y/H < 0.1$ region [11,15], the results for this region are not discussed and are only shown for completeness.

3. Results and Discussion

3.1. Turbulence Statistics

The velocity profile in the near-wall region for a smooth wall can be expressed with the following log law:

$$U^+ = \frac{1}{\kappa} \ln y^+ + B \tag{4}$$

where $\kappa = 0.41$ and $B = 5.5$.

In rough-wall conditions, the profiles of U shift downwards by ΔU^+ due to the roughness effects (Figure 2a), which can be expressed as follows:

$$U^+ = \frac{1}{\kappa} \ln(y + d)^+ + B - \Delta U^+ \tag{5}$$

where d is the zero-plane displacement from the roughness tops (Figure 1b), and ΔU^+ is the roughness function. The relative zero-plane displacement d/D was in the 0.15–0.3 range [33], and $d/D = 0.2$ was used in the present study, which is close to the value of 0.217 suggested by Defina [20] and the value of 0.19 suggested by Singh et al. [34]. ΔU^+ was related to Re_Δ, and the following relationship suggested by Ligrani and Moffat [35] was used:

$$\Delta U^+ = \left(\frac{1}{\kappa} \ln Re_\Delta{}^2 - 3.3\right) \times \sin[0.4258(\ln Re_\Delta - 0.811)] \tag{6}$$
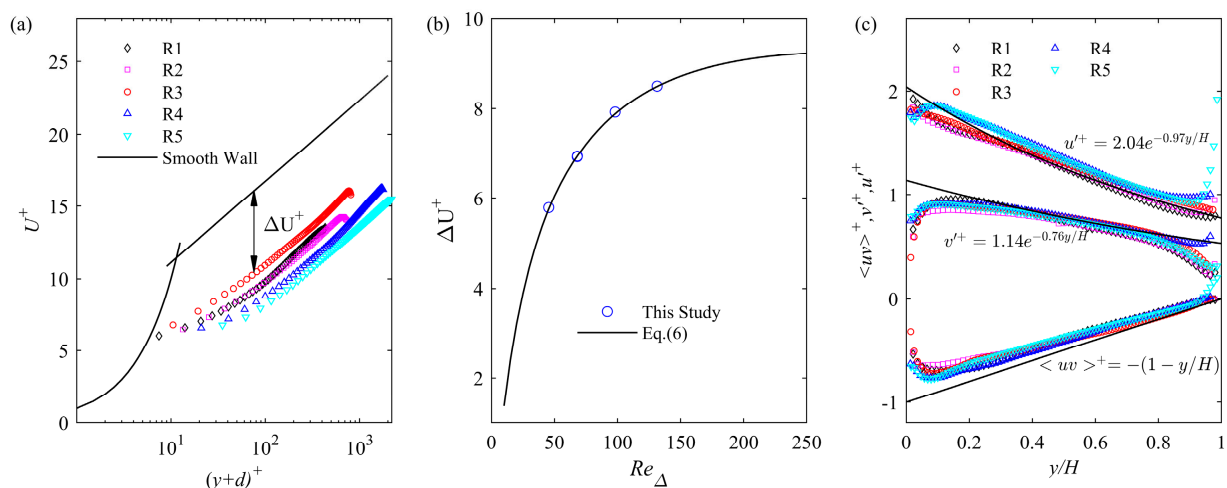

Figure 2. (**a**) Wall-normal profile of mean velocity. (**b**) Roughness function versus the roughness Reynolds number. (**c**) Wall-normal profiles of turbulence intensities and Reynolds stress.

The distributions of the streamwise and stream-normal turbulence intensities for a 2D uniform rough-bed OCF were as follows [36]:

$$u'^+ = D_u e^{-\lambda_u \frac{y}{H}} \qquad (7)$$

$$v'^+ = D_v e^{-\lambda_v \frac{y}{H}} \qquad (8)$$

where D_u, λ_u, D_v, and λ_v are constants. Kironoto and Graf [37] obtained D_u = 2.04, λ_u = 0.97, D_v = 1.14, and λ_v = 0.76, using least-squares fits to the experimental data for a rough-bed OCF. $u' = \sqrt{\overline{u^2}}$, $v' = \sqrt{\overline{v^2}}$, $u^2/2$ and $v^2/2$ represent the streamwise and wall-normal TKE, respectively, and Equations (7) and (8) show that the roots of twice the time-averaged TKE for rough-bed OCFs collapsed with each other when they were scaled by friction velocities.

The wall-normal profiles of the turbulence statistical parameters are shown in Figure 2, where the experimental data are well-described by Equations (5) and (6). The distributions of the turbulence intensities agreed reasonably well with Equations (7) and (8), and the Reynolds stress distribution in the outer region ($y/H \geq 0.2$) followed a linear trend, as shown in the figure. The abnormal distributions of the turbulence intensity and the Reynolds stress for R5 (Figure 2c) in the region close to the water surface ($y > 0.92H$) were due to the plexiglass sheet.

3.2. VLSM Scaling in Rough-Bed OCFs

The contour maps of the premultiplied spectra of the streamwise velocities are shown in Figure 3. For all the runs, the spectra exhibited double peaks for $y/H \geq 0.2$, with wavelengths at ~3 and ~20H, as shown in Figure 3 with the white lines. Compared with previous studies, it is evident that these were the large-scale motion (LSM) and VLSM wavelengths, respectively.

The wavelengths of LSMs and VLSMs are denoted with λ_{LSM} and λ_{VLSM}, respectively, and their variations along the entire water depth are shown in Figure 4, where the maximal VLSM wavelength for R4 was ~30H, which is much longer than the ~20H in the other runs. Cameron et al. [11] proposed three possible contributions to the VLSM scaling, i.e., B/H, H/Δ, and Re_τ. To unambiguously identify the dominant contributor, the maxima of λ_{VLSM} are listed in Table 3, and are plotted against B/H, H/D, and Re_τ in Figure 5a–c. For comparison, the experimental data for rough beds (published by Cameron et al. [11] and Zampiron et al. [38]) and for a smooth bed (published by Duan et al. [8]) are also reported. When calculating H/Δ, $\Delta = D$ was used in this study for consistency with the results reported by Cameron et al. [11], while $\Delta \approx 3.5\,k$ was set for the study by Zampiron et al. [38], who used a hook component with height $k \approx 1.1$ mm as the bed roughness. In addition, Δ was assumed to be 0.05 mm for a clear-glass bed [39] in the experiment of Duan et al. [8].

As Table 3 shows, comparing R3–R5 in this study in which B/H and H/Δ were invariant, while Re_τ varied significantly, shows that the VLSM wavelengths rarely changed. The possibility that Re_τ controlled the VLSM scale could be ruled out, which is consistent with the report of Peruzzi et al. [9]. Comparing R2 in this study with C2 (or C4) in the study by Duan et al. [8], the two runs had almost the same B/H but very different H/Δ, and the VLSM wavelengths were roughly the same. This result suggests that bed roughness probably does not play a role in controlling the VLSM wavelengths, at least for OCFs over bed types with smooth and large relative submergence. After ruling out the roles of H/Δ and Re_τ, B/H appeared to be the controlling scale. Moreover, Ferraro et al. [40] proposed the VLSM size as a function of B/H rather than H/Δ because no significant VLSM variation was observed in their study when Δ varied without varying B/H. However, in their study of flows with low relative submergence, no VLSM-associated peaks were observed.
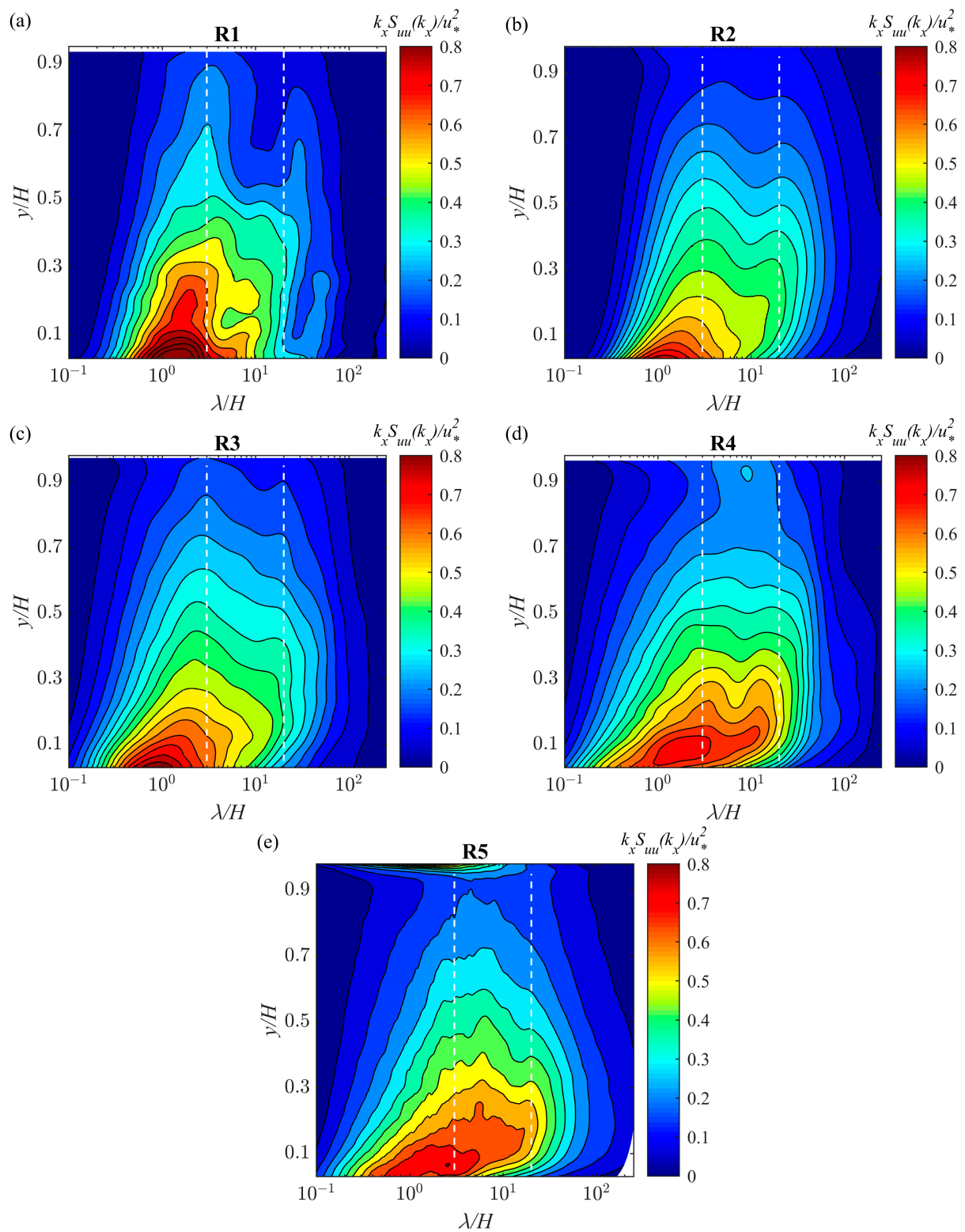
Figure 3. Premultiplied power spectra of streamwise velocity for runs: (**a**) R1, (**b**) R2, (**c**) R3, (**d**) R4 and (**e**) R5.
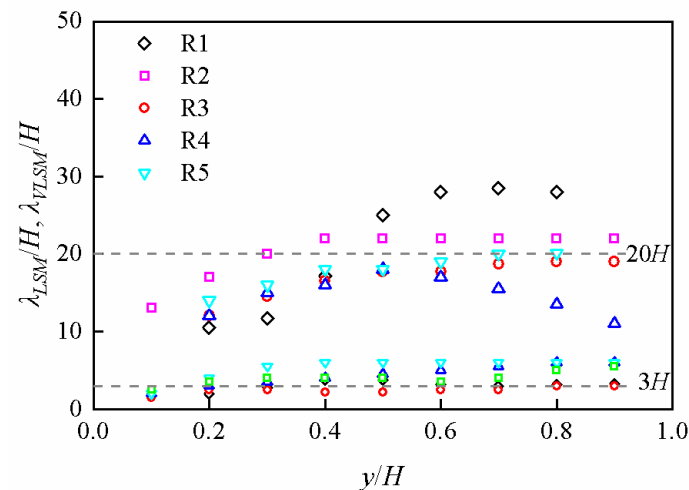
Figure 4. LSM and VLSM wavelengths represented by small and large symbols, respectively.

Table 3. Maximal VLSM wavelengths from different sources.

Author	Run	B/H	H/Δ	Re_τ	λ_{VLSM}/H
This study	R1	14.5	4.3	442	28.5
	R2	8.7	7.2	742	22.0
	R3	5.1	12.2	831	19.0
	R4	5.1	12.1	1879	18.0
	R5	5.1	12.3	2566	20.1
Cameron et al. (2017) [11]	H030	39.2	1.9	1140	50.7
	H050	23.5	3.1	1900	39.0
	H070	16.7	4.4	2670	30.9
	H095	12.4	5.9	3590	26.0
	H120	9.8	7.5	4540	22.1
Zampiron et al. (2020) [38]	s000	7.9	13.2	1360	25.3
Duan et al. (2020) [8]	C1	12	500	614	21.3
	C2	8.6	700	1030	23.1
	C3	9.1	660	1508	29.4
	C4	8.6	1300	1903	21.5
	C5	7.2	1560	2407	18.8

An intuitive comparison of the measured data with B/H, H/Δ, and Re_τ is shown in Figure 5a–c, respectively. The data generally fit the curve relating the VLSM wavelengths to B/H proposed by Cameron et al. [11] despite some experimental scatter at low B/H ratios while deviating significantly from those related to H/Δ and Re_τ. This phenomenon again suggests the importance of B/H in dominating the VLSM scale. The failure to predict λ_{VLSM} on the basis of H/Δ is evident (Figure 5b), particularly for the smooth OCF case. In this case, the curve fell below $3H$, which means that the VLSM wavelengths were even smaller than the LSM ones. Clearly, this is at odds with the facts and impossible.

3.3. VLSM Contributions to TKE and Reynolds Stress

$\lambda = 3H$ is widely used to separate LSMs and VLSMs on the basis of the premultiplied spectra of the streamwise velocities [4,5,8,10]. With scaling-based decomposition, Hu et al. [41] divided wall-attached eddies and very-large-scale wall-detached eddies (actually VLSM) with $\lambda = 3H$. Following this separation scale, the VLSM contributions to the TKE and Reynolds stress can be evaluated as follows:

$$\gamma_{u_i u_j} = \frac{\int_0^{2\pi/\lambda} S_{u_i u_j}(k_x)\,dk_x}{\int_0^\infty S_{u_i u_j}(k_x)\,dk_x} \tag{9}$$
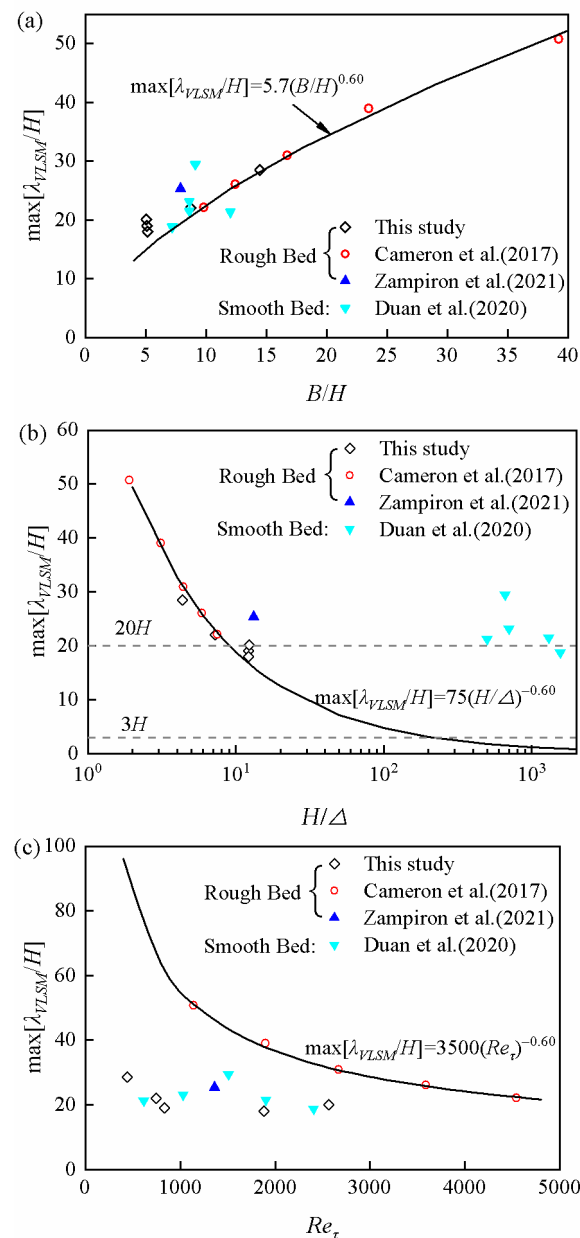
Figure 5. Maximal VLSM wavelengths versus (**a**) flow aspect ratio, (**b**) relative submergence, and (**c**) friction Reynolds number. The solid line shows the scaling relationship for the VLSM wavelengths proposed by Cameron et al. [11]. The experimental data for rough beds were from Cameron et al. [11] and Zampiron et al. [38] and the data for a smooth bed was from Duan et al. [8].

The variations in γ_{uu} and γ_{uv} with the flow depth are plotted in Figure 6. The data from run R2 were not used for the aforementioned reasons. Figure 6a shows that VLSMs contributed ~60% to the TKE, which is consistent with the contribution of 55–65% reported by Duan et al. [8]. For each run, γ_{uu} increased from the near-bed region until $0.5H$ and thereafter maintained a relatively stable value. In addition, an interesting feature is shown in Figure 6a. At the same water depth, γ_{uu} increased with Re_τ in the 0.1–$0.5H$ region, implying VLSMs are more fully developed in higher Re_τ flows. Given that nearly all hydraulic flows are high-Reynolds-number wall turbulence [19], an increasingly prominent role of VLSMs in the transport of momentum, energy, and mass is to be expected. This trend was also reported by Duan et al. [8] in their smooth-bed OCF study, as shown in Figure 5c. Figure 6b shows that the VLSMs contributed 38–50% to the Reynolds stress fraction, which is less than the reported contribution of 50–60% for smooth-bed OCFs. In

contrast to the variation in γ_{uu} with Re_τ, the variation in γ_{uv} showed no distinct trend, which is consistent with Yan et al. [7].
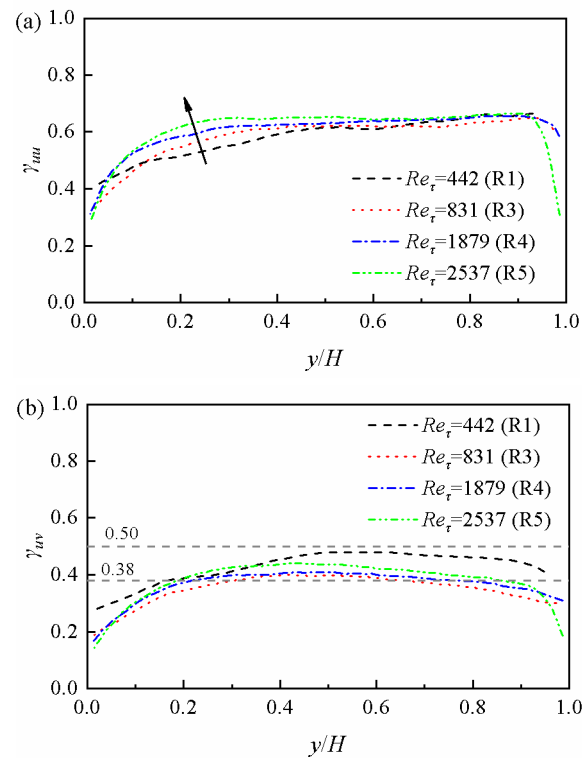

Figure 6. (**a**) Streamwise kinetic energy fraction and (**b**) Reynolds stress fraction contributed by VLSMs, using $3H$ as a separation scale.

The variations in γ_{uu} with Re_τ at $y/H = 0.2$ and 0.4 are shown in Figure 7. Evidently, γ_{uu} increased almost linearly with Re_τ. The slopes of the linear fits for $y/H = 0.2$ and 0.4 were 4.591×10^{-5} and 2.366×10^{-5}, respectively, suggesting that the growth of the VLSM fraction with Re_τ slowed down as the VLSMs developed towards the water surface.
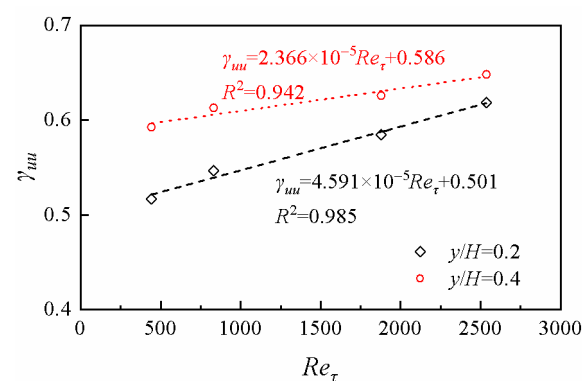

Figure 7. Streamwise kinetic energy fraction contributed by VLSMs versus the friction Reynolds number for $y/H = 0.2$ and 0.4.

In addition to $\lambda = 3H$, $\lambda = 20H$ was used as a separation scale to analyze the VLSM contributions to the TKE, given that the VLSM wavelengths in this study were around this scale; the result is shown in Figure 8. In contrast to the ~60% corresponding to $\lambda = 3H$ (Figure 6a), γ_{uu} corresponding to $\lambda = 20H$ dropped to ~20%, suggesting the sensitivity of the VLSM-contributed TKE to the separation scale. The difference between these two different separation scales was exactly the amount of the TKE carried by structures with

wavelengths in the 3–20H range, that is, ~40%. In addition, the tendency of γ_{uu} to increase with Re_τ is still present in Figure 8. Such a feature may signal a robust relationship between VLSMs and Re_τ.
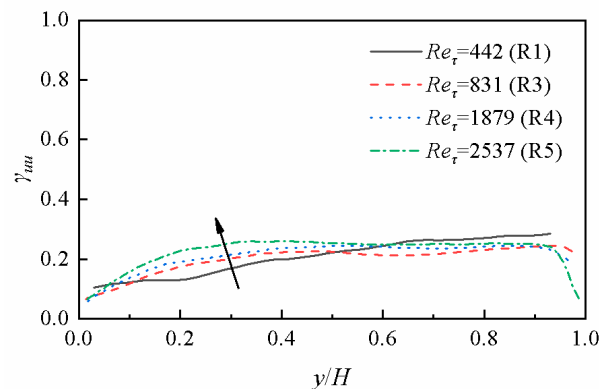

Figure 8. Streamwise kinetic energy fraction contributed by VLSMs using 20H as a separation scale.

4. Conclusions

This study experimentally investigated the scaling and energy contents of very-large-scale motions (VLSMs) in rough-bed OCFs. Distinct double peaks corresponding to LSMs and VLSMs in the premultiplied streamwise velocity spectra were observed for all runs in this study. The typical VLSM wavelengths in large-submergence rough-bed OCFs were around 20H, consistent with the results of previous studies.

A careful examination of the available measured VLSM length data suggested that the flow aspect ratio is key to controlling the VLSM scale rather than the relative submergence and friction Reynolds number. The role of the relative submergence was easily ruled out by comparing the VLSM scales of flows over smooth and rough beds.

Using 3H as a criterion for LSM/VLSM separation, the VLSM contributions to the TKE and Reynolds stress in rough-bed OCFs were reported for the first time, which were ~60% and 38–50%, respectively. In addition, the VLSM contribution to the TKE in the 0.1–0.5H range apparently increased with the friction Reynolds number in OCFs irrespective of bed roughness. Given that hydraulic flows are generally wall turbulence with a high Reynolds number, VLSMs could probably dominate the transport process in practical engineering.

Regarding the present study's focus on large-submergence flows, further studies are needed to elucidate VLSM differences for flows with various submergence or roughness levels.

Author Contributions: Conceptualization, Y.S. and J.L.; methodology, Y.S.; experiment, Y.S. and J.L.; data processing, Y.S. and S.Y.; writing—original draft preparation, Y.S.; writing—review and editing, S.Y.; visualization, Y.S.; supervision, J.L. All authors have read and agreed to the published version of the manuscript.

Data Availability Statement: The data that support the findings of this study are available from the corresponding author upon reasonable request.

Notation

B	flume width
D	particle diameter
d	zero-plane displacement from the roughness tops
Fs	sampling frequency of the velocity fields
$Fu_i(f)$	FT of u_i ($u_1 = u$, $u_2 = v$)
f	frequency of FT
H	water depth
J	bed slope
k	bed roughness height
k_x	streamwise wavenumber
$S_{u_i u_j}(f)$	power spectral density of $u_i u_j$ ($u_1 = u$, $u_2 = v$)
T	total image acquisition time
U	time-averaged velocity in the streamwise direction
U_m	depth-averaged velocity
u/v	fluctuating velocity in the streamwise or wall-normal direction
u'/v'	streamwise or wall-normal turbulence intensities
u_*	friction velocity
Fr	$U_m/(gH)^{0.5}$ = Froude number
Re	$U_m H/\nu$ = Reynolds number
Re_τ	$u_* H/\nu$ = friction Reynolds number
Re_Δ	$u_* \Delta/\nu$ = roughness Reynolds number
x/y	streamwise or wall-normal direction
ν	kinematic viscosity
Δ	equivalent roughness
$\Delta x/\Delta y$	vector spacing in the streamwise or wall-normal direction
ΔT	$1/Fs$ = time interval between successive velocity fields
ΔU^+	roughness function
$\gamma_{u_i u_j}(f)$	VLSM contributions to the TKE and Reynolds stress ($u_1 = u$, $u_2 = v$)
λ	wavelength

References

1. Lee, J.; Ahn, J.; Sung, H.J. Comparison of Large- and Very-Large-Scale Motions in Turbulent Pipe and Channel Flows. *Phys. Fluids* **2015**, *2*, 25101. [CrossRef]
2. Lee, J.H.; Sung, H.J. Comparison of Very-Large-Scale Motions of Turbulent Pipe and Boundary Layer Simulations. *Phys. Fluids* **2013**, *4*, 45103. [CrossRef]
3. Hellström, L.H.O.; Sinha, A.; Smits, A.J. Visualizing the Very-Large-Scale Motions in Turbulent Pipe Flow. *Phys. Fluids* **2011**, *1*, 11703. [CrossRef]
4. Balakumar, B.J.; Adrian, R.J. Large- and Very-Large-Scale Motions in Channel and Boundary-Layer Flows. *Philos. Trans. R. Soc. A Math. Phys. Eng. Sci.* **2007**, *1852*, 665–681. [CrossRef] [PubMed]
5. Guala, M.; Hommema, S.E.; Adrian, R.J. Large-Scale and Very-Large-Scale Motions in Turbulent Pipe Flow. *J. Fluid. Mech.* **2006**, *554*, 521–542. [CrossRef]
6. Lee, J.H.; Sung, H.J. Very-Large-Scale Motions in a Turbulent Boundary Layer. *J. Fluid. Mech.* **2011**, *673*, 80–120. [CrossRef]
7. Yan, Z.; Duan, Y.; Zhu, D.; Li, D. Characteristics of Very-Large-Scale Motions in Gradually Varied Open-Channel Flows Upstream of a Run-of-River Dam. *Phys. Fluids* **2022**, *9*, 095123. [CrossRef]
8. Duan, Y.; Chen, Q.; Li, D.; Zhong, Q. Contributions of Very Large-Scale Motions to Turbulence Statistics in Open Channel Flows. *J. Fluid. Mech.* **2020**, *892*, A3. [CrossRef]
9. Peruzzi, C.; Poggi, D.; Ridolfi, L.; Manes, C. On the Scaling of Large-Scale Structures in Smooth-Bed Turbulent Open-Channel Flows. *J. Fluid. Mech.* **2020**, *889*, A1–A25. [CrossRef]
10. Zhang, P.; Duan, Y.; Li, D.; Hu, J.; Li, W.; Yang, S. Turbulence Statistics and Very-Large-Scale Motions in Decelerating Open-Channel Flow. *Phys. Fluids* **2019**, *12*, 125106.
11. Cameron, S.; Nikora, V.; Stewart, M. Very-Large-Scale Motions in Rough-Bed Open-Channel Flow. *J. Fluid. Mech.* **2017**, *814*, 416–429. [CrossRef]
12. Scherer, M.; Uhlmann, M.; Kidanemariam, A.; Krayer, M. On the Role of Turbulent Large-Scale Streaks in Generating Sediment Ridges. *J. Fluid. Mech.* **2022**, *930*, A11. [CrossRef]

13. Schobesberger, J.; Worf, D.; Lichtneger, P.; Yücesan, S.; Hauer, C.; Habersack, H.; Sindelar, C. Role of Low-Order Proper Orthogonal Decomposition Modes and Large-Scale Coherent Structures On Sediment Particle Entrainment. *J. Hydraul. Res.* **2021**, *60*, 1–17. [CrossRef]

14. Cameron, S.; Nikora, V.; Witz, M. Entrainment of Sediment Particles by Very Large-Scale Motions. *J. Fluid. Mech.* **2020**, *888*, A7. [CrossRef]

15. Stewart, M.T. Turbulence Structure of Rough-Bed Open-Channel Flow. Doctoral Dissertation, University of Aberdeen, Aberdeen, UK, 2014.

16. Grass, A.J. Structural Features of Turbulent Flow Over Smooth and Rough Boundaries. *J. Fluid. Mech.* **1971**, *2*, 233–255. [CrossRef]

17. Dwivedi, A.; Melville, B.W.; Shamseldin, A.Y.; Guha, T.K. Analysis of Hydrodynamic Lift On a Bed Sediment Particle. *J. Geophys. Res.-Earth* **2011**, *116*, F2. [CrossRef]

18. Thielicke, W.; Sonntag, R. Particle Image Velocimetry for Matlab: Accuracy and Enhanced Algorithms in Pivlab. *J. Open Res. Softw.* **2021**, *1*, 1–14. [CrossRef]

19. Adrian, R.J.; Marusic, I. Coherent Structures in Flow Over Hydraulic Engineering Surfaces. *J. Hydraul. Res.* **2012**, *5*, 451–464. [CrossRef]

20. Defina, A. Transverse Spacing of Low-Speed Streaks in a Channel Flow Over a Rough Bed. In *Coherent Flow Structures in Open Channels*; Ashworth, P.J., Bennett, S.J., Best, J.L., Mclellandm, S.J., Eds.; John Wiley & Sons Ltd.: London, UK, 1996; pp. 87–99.

21. Nikora, V.; Goring, D.; Mcewan, I.; Griffiths, G. Spatially Averaged Open-Channel Flow Over Rough Bed. *J. Hydraul. Eng.* **2001**, *2*, 123–133. [CrossRef]

22. Adrian, R.J. Particle-Imaging Techniques for Experimental Fluid Mechanics. *Annu. Rev. Fluid. Mech.* **1991**, *23*, 261–304. [CrossRef]

23. Duan, Y.; Zhang, P.; Zhong, Q.; Zhu, D.; Li, D. Characteristics of Wall-Attached Motions in Open Channel Flows. *Phys. Fluids* **2020**, *5*, 55110.

24. Monty, J.P.; Hutchins, N.; Ng, H.C.H.; Marusic, I.; Chong, M.S. A Comparison of Turbulent Pipe, Channel and Boundary Layer Flows. *J. Fluid. Mech.* **2009**, 431–442. [CrossRef]

25. Hutchins, N.; Marusic, I. Large-Scale Influences in Near-Wall Turbulence. *Philos. Trans. R. Soc. A Math. Phys. Eng. Sci.* **2007**, *1852*, 647. [CrossRef] [PubMed]

26. Adrian, R.J. Hairpin Vortex Organization in Wall Turbulence. *Phys. Fluids* **2007**, *4*, 41301. [CrossRef]

27. Kim, K.C.; Adrian, R.J. Very Large-Scale Motion in the Outer Layer. *Phys. Fluids* **1999**, *2*, 417–422. [CrossRef]

28. Taylor, G.I. The Spectrum of Turbulence. *Proc. R. Soc. Lond. Ser. A Math. Phys. Sci.* **1938**, *919*, 476–490. [CrossRef]

29. Wickersham, A.J.; Li, X.; Ma, L. Comparison of Fourier, Principal Component and Wavelet Analyses for High Speed Flame Measurements. *Comput. Phys. Commun.* **2014**, *4*, 1237–1245. [CrossRef]

30. Li, Z.; Li, C. Non-Gaussian Non-Stationary Wind Pressure Forecasting Based On the Improved Empirical Wavelet Transform. *J. Wind Eng. Ind. Aerod.* **2018**, *179*, 541–557. [CrossRef]

31. Mariotti, A. Axisymmetric Bodies with Fixed and Free Separation: Base-Pressure and Near-Wake Fluctuations. *J. Wind Eng. Ind. Aerod.* **2018**, *176*, 21–31. [CrossRef]

32. Perna, R.; Abela, M.; Mameli, M.; Mariotti, A.; Pietrasanta, L.; Marengo, M.; Filippeschi, S. Flow Characterization of a Pulsating Heat Pipe through the Wavelet Analysis of Pressure Signals. *Appl. Therm. Eng.* **2020**, *171*, 115128. [CrossRef]

33. Nezu, I.; Nakagawa, H. *Turbulence in Open-Channel Flows*; CRC Press: Rotterdam, The Netherlands, 1993.

34. Singh, K.M.; Sandham, N.D.; Williams, J.J.R. Numerical Simulation of Flow Over a Rough Bed. *J. Hydraul. Eng.* **2007**, *4*, 386–398. [CrossRef]

35. Ligrani, P.M.; Moffat, R.J. Structure of Transitionally Rough and Fully Rough Turbulent Boundary Layers. *J. Fluid. Mech.* **1986**, *162*, 69–98. [CrossRef]

36. Nezu, I. Turbulent Intensities in Open-Channel Flows. *Proc. Jpn. Soc. Civ. Eng.* **1977**, *261*, 67–76. [CrossRef]

37. Kironoto, B.A.; Graf, W.H. Turbulence Characteristics in Rough Uniform Open-Channel Flow. *Proc. Inst. Civ. Eng.-Water Marit. Energy* **1994**, *4*, 333–344. [CrossRef]

38. Zampiron, A.; Cameron, S.; Nikora, V. Secondary Currents and Very-Large-Scale Motions in Open-Channel Flow Over Streamwise Ridges. *J. Fluid. Mech.* **2020**, *887*, A17. [CrossRef]

39. Auel, C.; Albayrak, I.; Sumi, T.; Boes, R.M. Sediment Transport in High-Speed Flows Over a Fixed Bed: 1. Particle Dynamics. *Earth Surf. Proc. Land* **2017**, *9*, 1365–1383. [CrossRef]

40. Ferraro, D.; Coscarella, F.; Gaudio, R. Scales of Turbulence in Open-Channel Flows with Low Relative Submergence. *Phys. Fluids* **2019**, *12*, 125114. [CrossRef]

41. Hu, R.; Yang, X.I.A.; Zheng, X. Wall-Attached and Wall-Detached Eddies in Wall-Bounded Turbulent Flows. *J. Fluid. Mech.* **2020**, *885*, A30. [CrossRef]